THE 24TH CHESAPEAKE SAILING YACHT SYMPOSIUM
ANNAPOLIS, MARYLAND, JUNE 2022

Wingsail Profile Optimisation Using Computationally Efficient Methods

William Birch-Tomlinson, University of Southampton, Southampton, UK
Prof Stephen Turnock, University of Southampton, Southampton, UK
Dr Martyn Prince, Wolfson Unit, Southampton, UK

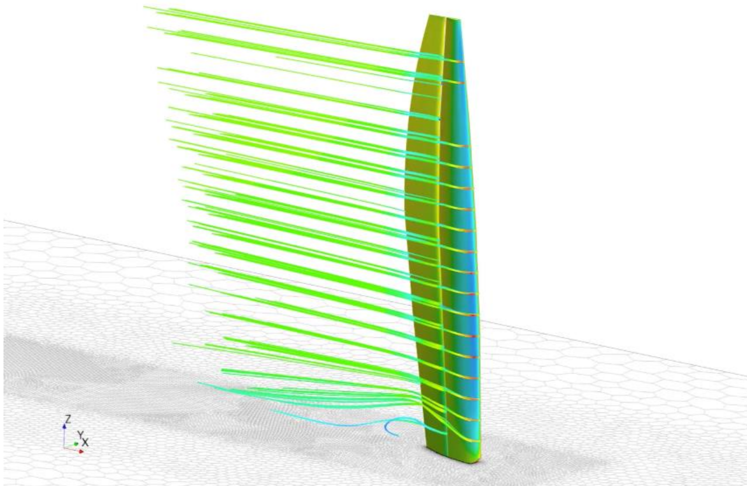

ABSTRACT

On any race yacht, having the ability to maximise boat speed is key to obtain race winning performances. To achieve this the sail or wing must be set at its optimum profile. To find the best wingsail profile the trend recently has been towards more computationally expense approaches, but can we use less intensive methods to contribute to the design and optimisation process when time and resource may be limited? With an extensive number of different flying shapes, a computationally efficient approach at accurately finding optimum wingsail profiles for any given wind speed and direction is required. Using a two-dimensional section of the wingsail, lift and drag characteristics were found using Reynolds Averaged Navier-Stokes (RANS) simulations within Star-CCM+. A modified lifting line (LL) model was programmed in Python which used the two-dimensional characteristics to give fast and accurate predictions of drive force and heeling moment for a twisted inflow. The LL code was verified using experimental data, and showed that with analytical corrections, accurate predictions of lift and induced drag could be obtained. 3D RANS simulations confirmed that the LL model with correct tuning of the root vortices could predict driving forces and heeling moments within 1% and 5% respectively for a typical range of angle of attacks (AoA) and wing shapes. LL predictions took ~8 seconds on a laptop compared to ~6 hours for 3D RANS simulations running on a High-Performance Computing cluster. A machine learning algorithm using Kernel ridge multivariate regression was trained to produce a surrogate model of the wingsail giving accurate predictions within 1% of the LL results. Using the surrogate model, performance predictions could be obtained in ~0.001 seconds showcasing the large computational savings. This method permitted an exhaustive search of different wingsail profiles, giving information on parameter trends such as AoA, camber, and twist. This provides a tool that could be adopted in a velocity prediction program (VPP) and used by sailors or designers to aid in the setup and trimming of wingsails for maximum performance.

NOTATION

AWA	Apparent wind angle (°)
AWS	Apparent wind speed (m s^{-1})
AoA	Angle of Attack (°)
β	Local flap angle w.r.t main element chord (°)

CFD Computational Fluid Dynamics
C_i Local chord (m)
C_D Coefficient of drag
C_L Coefficient of lift
C_M Coefficient of moment
CoE Centre of effort
D Drag force (N)
F_D Drive force (N)
F_S Side force (N)
h Height of CoE above origin (m)
HPC High Performance Computer
H_M Heeling moment (N m)
L Lift fore (N)
LL Lifting Line
L/D Lift to drag ratio
RANS Reynolds Averaged Navier-Stokes
Re Reynolds Number
TWA True wind angle (°)
TWS True wind speed (m s^{-1})
Γ Vortex strength (m^{-3} s^{-1})
u Incident flow velocity (m s^{-1})
VPP Velocity Prediction Programme
V_{indC} Induced velocity at point P_C (m s^{-1})
Z_C Vertical collocation point position (m)

INTRODUCTION

Ever since the successful 27th America's Cup (AC) win by Stars and Stripes in 1988 wingsails have been showcased to the sailing world on scale. Such devices featured in the 33rd, 34th and 35th AC and more recently SailGP on the F50 catamaran. Wingsails have several advantages over conventional soft sails by having higher aerodynamic efficiency, improved control, and the added ease of profile measurement (Whidden & Levitt, 2016). The wingsail on the F50 is controlled by a wing sheet that changes the angle of attack (AoA) of the wing, and buttons that effect camber, twist, and twist profile. Therefore, knowing optimum target wing profiles for a given true wind speed (TWS) and angle (TWA) allow teams to maximize boat speed and race performance. To accelerate the development of new teams, tools for helping them optimize and understand the boats performance are vital.

Recent advances in computational fluid dynamics (CFD) provide accurate tools for evaluating the forces and moments a wingsail produces, however, this accuracy comes at a computational cost by demanding more resource and time. An example of this is highlighted by Team New Zealand who used a 567 core Dell high performance computing (HPC) cluster to run RANS simulations to create an aerodynamic database during the 34th AC (Collie, et al., 2015). Therefore, unless you have the resource of a Cup team, 3D CFD is not often feasible for full design space exploration.

To reduce computational cost a lifting line (LL) model can be used to approximate the lift distribution and hence forces on a full 3D wingsail. A modified LL model using an iterative approach to make use of non-linear lift coefficients obtained from 2D RANS has been shown to give close agreements of drive force (F_D) and heeling moment (H_M) when compared to 3D RANS simulations at low AoA (Graf, et al., 2014). Graf found slight overpredictions of lift close to maximum lift coefficient (C_L) because LL theory struggles to capture the complex flow separation that occurs near stall. Graf used the model to optimise wingsail trim settings such as sheeting angle and camber using the 'Generalised Reduced Gradient' solver within Microsoft Excel, however, the optimisation was conducted for a wing with fixed AWA and twist.

To truly find the best wingsail profile, all configurations must be considered, hence the design space is greatly increased, therefore, an approach focused on computational speed is needed. Once 2D lift and drag coefficients have been obtained from CFD, the LL model can be tuned using a free vortex weighting at the root and necessary corrections to best correlate it to 3D CFD results. Predictions can be made in a few seconds compared to hours needed for 3D CFD giving huge savings. However, to compare thousands of different profiles an even faster tool is needed. This is where the use of a trained machine learning model will be introduced. A machine learning algorithm using Kernel ridge regression was trained to interpolate the relationship between AoA, camber, twist, F_D, side force (F_S), and H_M. The resulting surrogate model permitted an exhaustive search of different wingsail profiles, providing information on parameter trends such as AoA, camber, and twist. Wingsail profiles that exceeded a given heeling moment limit were excluded and the profile that maximized drive force was chosen to be optimal for that given TWS and TWA, see Figure 1.

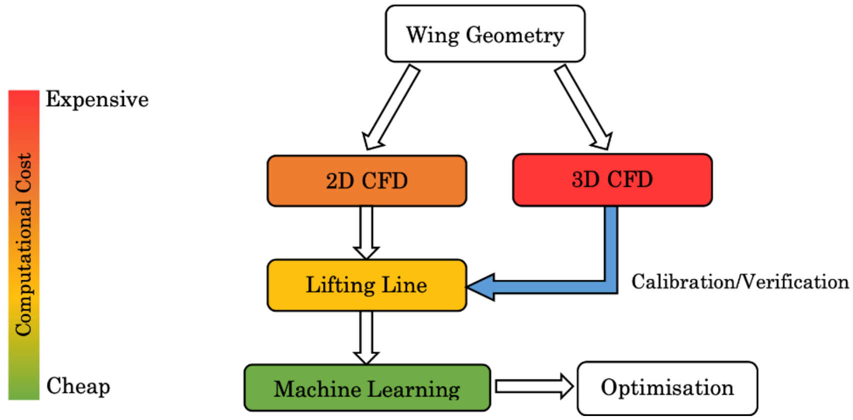

Figure 1 - Hierarchical approach to evaluating wingsail profiles

The method can be applied to other sailing yachts with similar sail plans. The combined use of a LL model and machine learning to produce surrogate models is shown to be valuable for the use in velocity prediction programmes (VPPs) (Peart, et al., 2021). The approach is not seen as a substitute for accuracy and resolution afforded using 3D RANS, but as a tool that could be 'practically' applied as part of a yacht's performance development process in terms of costs and timescales. The method is shown to have the 'potential' to bring good/reasonably accurate predictions to teams without so much dependency in terms of time, licensing cost, and computation resource for extensive 3D RANS.

WINGSAILS

Wingsails consist of two symmetrical airfoils: a leading-edge element and trailing edge flap. A cross-section of the wingsail and its terminology is shown in Figure 2. The 24 m wingsail on the F50 catamaran from SailGP is chosen for analysis. The wing has 5 hydraulic control arms that control 4 trailing edge flaps. The chord length varies along the span, with an equal chord distribution between the leading and trailing elements. The trailing edge flap rotates about a point which is 90% along the leading elements chord. Camber refers to the flap angle (β) at the root of the wing, and twist is the difference between β at the root and tip. The twist profile distribution is controlled by a Bezier curve meaning non-linear profiles are possible, however, for this investigation a linear profile was used.

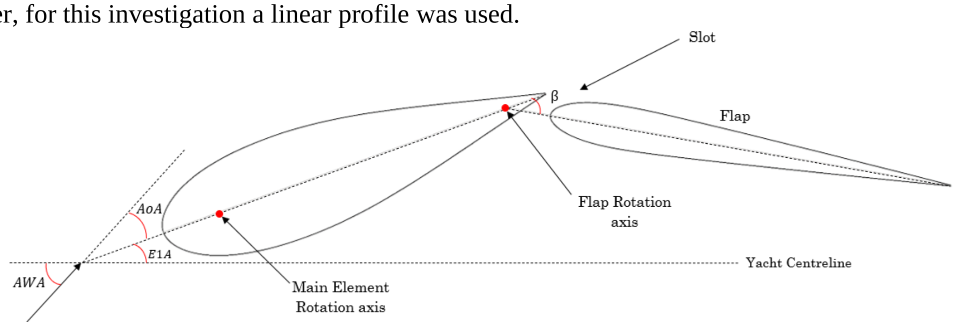

Figure 2 – Wingsail section terminology

THEORETICAL METHOD

Physics of Sailing

The forces created by the wingsail are resolved in the x and y directions of the boat coordinate system, as shown in Figure 3. Lift is defined as the component of the aerodynamic force (F_A) perpendicular to the onset flow direction (Houghton, 2013). Drag is the component of F_A in the direction of the onset flow. Yachts encounter a twisted incident wind due to earths boundary layer meaning that both apparent wind speed (AWS) and apparent wind angle (AWA) change with height. Therefore, lift and drag are resolved into F_D and F_S:

$$F_D = L\, sin(AWA) - D\, cos(\mathrm{AWA})$$

$$F_S = L\, cos(\mathrm{AWA}) + D\, sin(AWA)$$

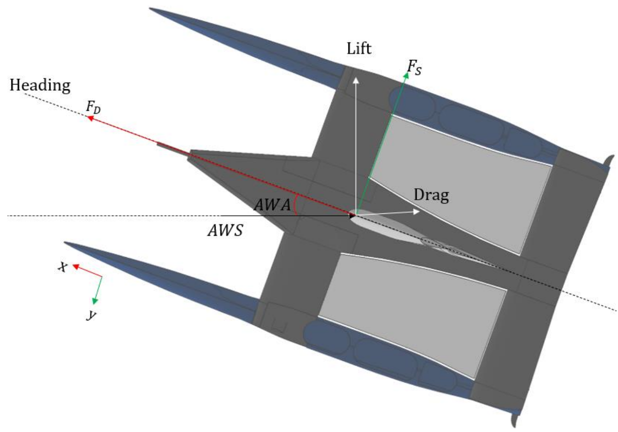

Figure 3 - Plan view of aerodynamic forces acting on the wing

F_A is simplified to act at a single point on the sail plan called the centre of effort (CoE). The position of this is dependent on many factors adjusted by sail trim. The vertical height of the CoE above the mast ball is denoted by h. This force induces a moment around the mast ball causing the yacht to heel. This is labelled H_M:

$$H_M = F_S \times h$$

Upwind Requirements

This paper will focus on upwind sailing, i.e. $TWA < 90^{\circ}$, to limit the number of optimisation cases, but the methods are also appliable to downwind cases. It is reasonable to assume that when foiling upwind F_D is to be maximised without exceeding a maximum H_M constraint. This approximation neglects the induced hydrodynamic drag created by F_S. The side force is balanced by the appendages in the water, therefore high values of F_S create large amounts of hydrodynamic drag. Ultimately F_S causes the boat to sail with leeway. In stronger winds, to obtain large drive forces without exceeding the H_M constraint, wingsail inversion is used to give a negative camber at the top of the sail providing desirable righting moment R_M (Whidden & Levitt, 2016). The control arms make it possible for the wing trimmer to easily add negative twist at the top of the wing. Wingsail inversion has been proven to obtain the best F_D/H_M ratio for strong wind conditions (Wood & Tan, 1978).

Computational Fluid Dynamics

The commercial software package Star-CCM+ 2020.3 has been chosen as the fluid dynamics solver in this study. Star-CCM+ is widely used throughout the marine industry and provides an integrated environment for computer aided design (CAD) import, geometry repair, automated meshing, post-processing, and design exploration.

2D Analysis

A cross-section of the F50 wing with maximum chord length of 4.9 m was used for the 2D section analysis. An AWS of 40 knts was chosen for an upwind sailing case in approximately 16 knts TWS. The calculated Re number is 6.85×10^6, using combined chord as the length scale. The air properties used for the 2D simulations are standard air properties taken at sea level, see Table 1. A design sweep of AoA and β were conducted using the Design Manager tool within Star-CCM+. A domain study was carried out resulting in a chosen domain size of 4 chords upstream/either side and 8 chords downstream of the mast ball coordinate. At this size the change in drag coefficient (C_D) and C_L with respect to increased domain size had converged to < 2%. The boundary conditions were setup with a velocity inlet, pressure outlet and symmetry boundary conditions on the sides.

Table 1 – Air properties used for 2D simulation at sea level and 15 $^{\circ}C$

Property	
Pressure	$101.3 \times 10^3\ N\ m^{-2}$
Density	$1.225\ kg\ m^{-3}$
Dynamic Viscosity	$1.802 \times 10^{-5}\ N\ s\ m^{-2}$
Flow Speed	$20.578\ m\ s^{-1}$

Table 2 presents the assumptions and appropriate parameters used for the simulation setup. Unsteady RANS simulations have been conducted with 1st order time integration, and a time step of 0.015 seconds to better solve the N-S equations and achieve accurate results. A maximum physical simulation time of 8.5 seconds has been chosen which allows a flow particle in the free stream to travel approximately 3 times the domain length. The SST k-ω model (Menter, 1994) was chosen after reviewing previous literature regarding aerodynamic wingsail analyses (Collie, et al., 2015). Comparing different models was beyond the scope of this project therefore the SST k-ω model was chosen for both 2D and 3D simulations.

Table 2 - Simulation assumptions used for 2D CFD

Category	Model
Time	Implicit Unsteady
Time step	0.015 s
Max physical time	8.5 s
Flow	Segregated flow
Equation of state	Constant density
Viscous Regime	Turbulent
Turbulence model	$SST\ (Menter)\ k-\omega$
Wall treatment	All y^+
Turbulence intensity	1%

Following the domain study, a mesh sensitivity analysis was undertaken to obtain grid-invariant simulation results. A polygonal mesher within Star-CCM+ was chosen because polygonal mashers are numerically more stable and give higher accuracy compared to an equivalent tetrahedral mesh (Siemens Digital Industries Software, 2020). A base size of 0.3 m was chosen, equating to approximately 155000 cells, as this provided a good balance between accuracy and solver time.

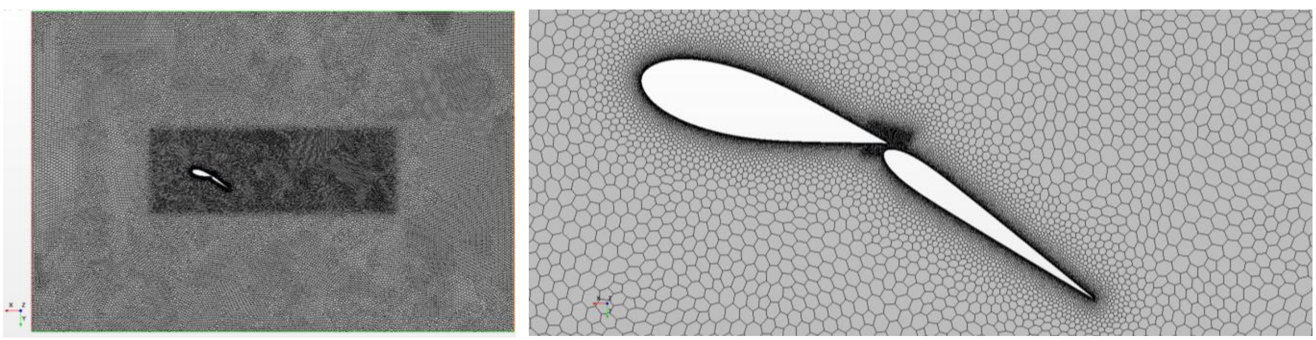

Figure 4 - Domain and mesh used for 2D analysis

An inner region sized 1 chord upstream, 1 chord either side and 5 chords downstream were used for mesh refinement with the target size being set to 50% of base size, see Figure 4. A second area of refinement was added around the wing profile and in the slot, seen in Figure 4. The boundary layer has been resolved to a $y^+ \approx 1$ using 20 structured prism layers to yield more accurate C_L and C_D values. The prism layers were defined by a starting layer thickness of 1.5×10^{-5} m and growth rate of 1.2. The first cell height has been chosen to lie within the desired y^+ range to reduce errors related to the wall functions used. Final mesh properties are shown in Table 3.

Table 3: Mesh properties used in 2D analysis

Property	
Base size	0.3 m
Cell no.	156893
Prism layer no.	20
Volume Refinement	50% of base
Slot refinement	2.5% of base
Airfoil refinement	0.8%

Validation was achieved by comparing results from the chosen CFD setup with experimental data from a wind tunnel test of a NACA0012 airfoil at a Reynolds number (Re) of 1.76×10^6 (Sheldehl & Klimas, 1981). The NACA0012 profile was simulated using the same Re number, domain, mesh, and setup used in the 2D analysis. In conclusion, the setup was found to provide accurate lift and drag predictions within the linear region, however, the values close to and around stall must be viewed with caution as the turbulence model fails to capture the complex wake and shed vortices present. Results can be seen in Figure 5.

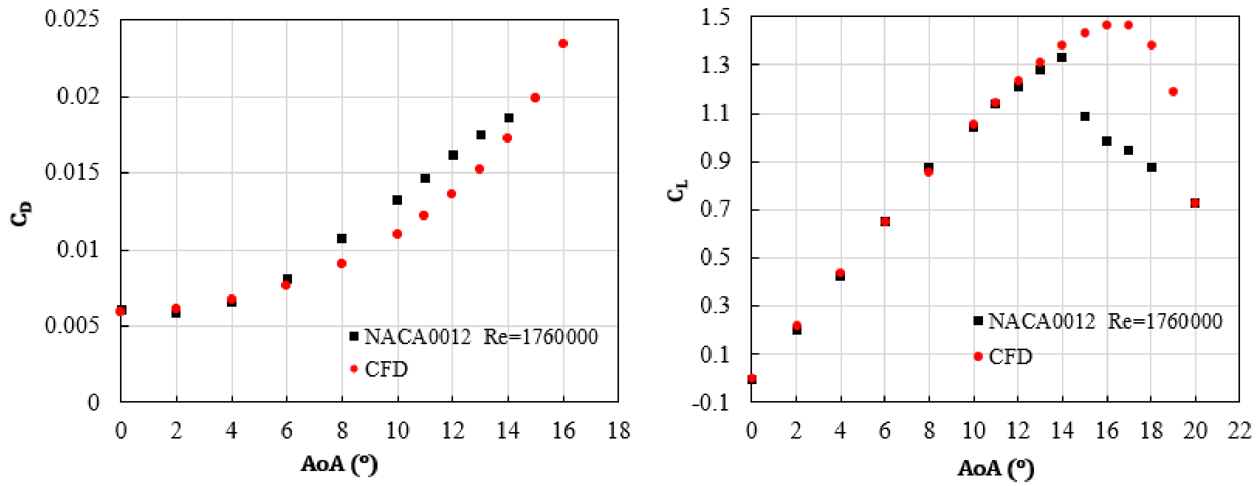

Figure 5 – Validation of 2D setup against NACA0012 airfoil

3D Analysis

Due to time constraints, full mesh and domain sensitivity analyses were not able to be conducted, but the simulation assumptions and models used were the same as that in the 2D analysis. Differences were a coarser mesh and smaller time step due to computational limits. Meshing was conducted using the University of Southampton's Iridis 5 HPC cluster using three nodes with 2.0 GH_z Intel Xeon processors totaling 120 cores and 486 GB Ram. A typical simulation took ~6 hours. The wing shape was manipulated in the CAD software package Rhino via a Grasshopper script. Throughout this study the aeroelastic effects of the wing have been neglected for simplicity. The domain size was increased from the 2D section simulations to 5 chords upstream, 5 chords either side, and 10 chords downstream to ensure there was no reversed flow on the boundaries. The domain height was 28.5 m which equated to 1 chord length above the wing tip, as shown in Figure 6.

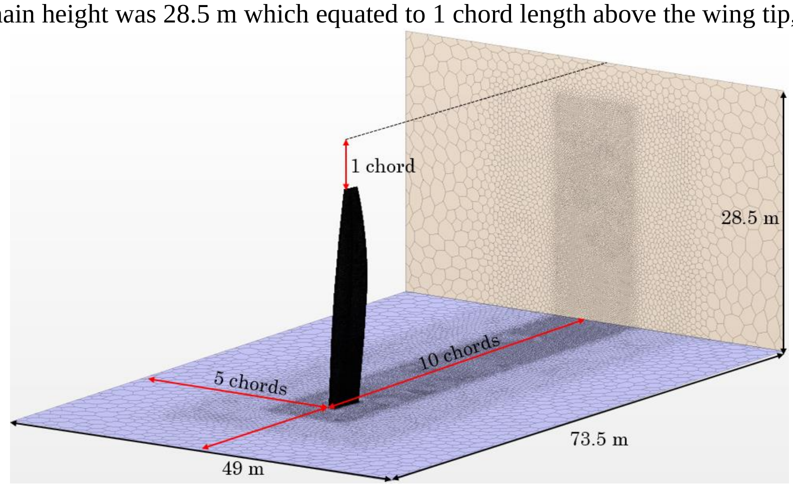

Figure 6 – 3D domain and mesh in Star-CCM+

Boundary conditions were as follows: a velocity inlet, pressure outlet, outlet on sides and top. For simplicity, the wing platform was not considered in the analysis, therefore as an acceptable assumption, the floor was modelled as a symmetry plane. For initial comparisons with the LL, the velocity gradient of the wind was ignored to simplify the setup. Table 4 shows the models used in the simulations.

Table 4 – Simulation assumptions used for 3D CFD

Category	Model
Time	Implicit Unsteady
Time step	0.1 s
Max physical time	8.5 s
Flow	Segregated flow
Equation of state	Constant density
Viscous Regime	Turbulent
Turbulence model	$SST\ (Menter)\ k-\omega$
Wall treatment	All y^+
Turbulence intensity	1%

Final 3D simulations were run with a twisted incident flow to replicate the true apparent wind the wing experiences when sailing. The twisted velocity gradient was achieved using field functions within Star-CCM+ and changes to the inflow boundaries were made to ensure simulations converged. A base size of 2 m was used with refinements around the wing, and on the wing surface itself to accurately capture the curved surface of the leading edge. Figure 8 shows the mesh refinement on the wing surface. A cross section of the wing at 12 m was taken to inspect the mesh around the wingsail seen in Figure 8. A total of 15 prism layers were used to resolve the boundary layer and no mesh refinement was used in the region of the slot to save time and computational cost. Even with a coarse base size of 2 m, the number of cells exceeded 20 million. Table 5 shows a summary of the mesh properties.

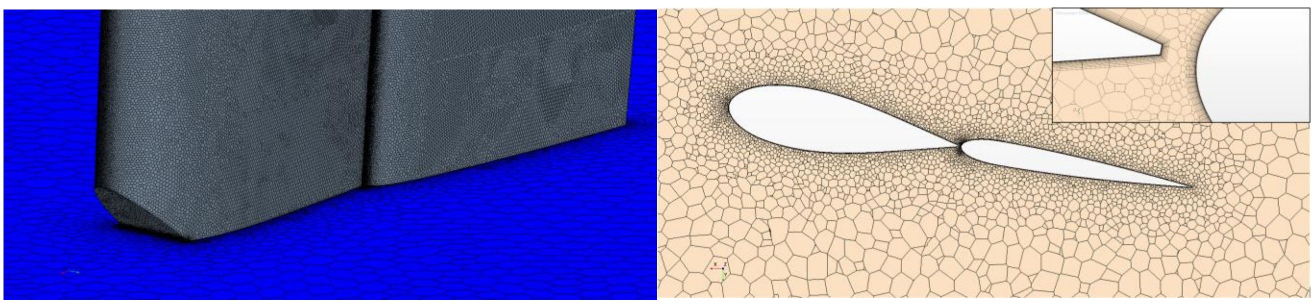

Figure 8 – Mesh at wing root and cross-section of mesh in 3D domain

Table 5 – Mesh properties used in 3D analysis

Property	
Base size	2.0 m
Cell no.	20.9 million
Prism layer no.	15
Volume Refinement 1	30% of base
Volume Refinement 2	10% of base
Airfoil refinement	1%

Lifting Line Theory

LL theory is a simple method of quickly establishing the performance of an airfoil. The method has the advantage that is provides good estimates of spanwise loading and induced drag, whilst remaining simple to implement and computationally inexpensive (Molland & Turnock, 2021). Flow around an airfoil can be represented by a combination of free stream and vortex flow circulations around the airfoil. This vortex can be represented by a line vortex of strength (Γ), called a lifting line, lying perpendicular to the chord (Claughton, 1998). The Kutta-Joukowski theorem states that the force (F) on this vortex is given by:

$$F = \rho U \times \Gamma$$

This only calculates the lift force perpendicular to the direction of the incoming flow, and neglects drag. By expanding the lifting vortex from the Kutta-Joukowski theorem, a bound vortex filament along the span of the wing is created. This vortex filament is extended to infinity along the incident flow to form a horseshoe vortex at the wing tips to comply with Thompson's rule. A change in lift along the span (y) can be represented by changing the strength of the bound vortex and any associated shedding of differential velocity through a free vortex filament (Γ_{fvf}).

$$\Gamma_{fvf} = \frac{d\Gamma}{dy}$$

The Biot-Savart law states that shed vorticity induces a velocity normal to the incident flow and that reduces the effective AoA. The net effect is a downwash which is added to the freestream velocity and causes the inflow to rotate. This induced velocity causes induced drag and is used to model the three-dimensional flow effects around an airfoil. Graf showed that a wingsail can be accurately modelled using a modified LL method described below. The wing is discretized into N number of panels depicted in Figure 9. Induced velocity is calculated in the centre of each panel from $j = 1,2 \ldots N$ by summing up the induced wind generated by any free vortex wake sheet and the discrete vortex filaments at root and tip (Graf, et al., 2014).

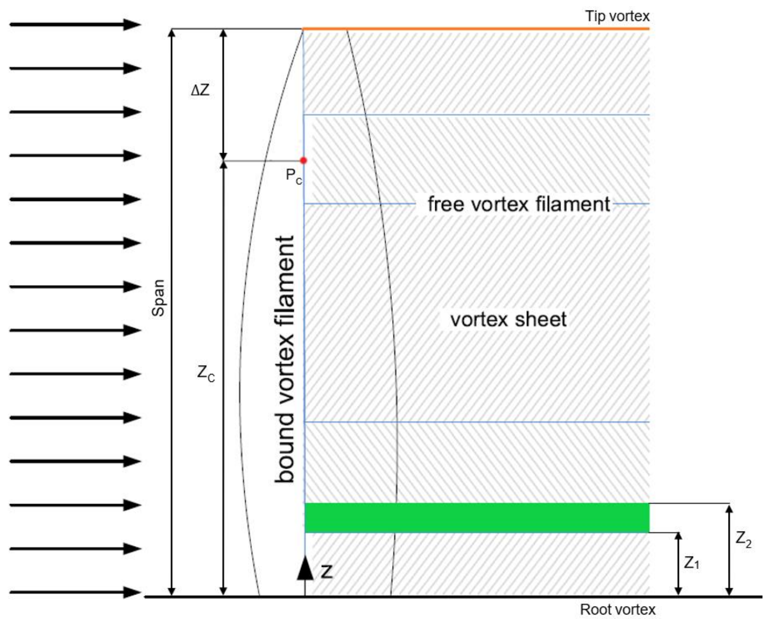

Figure 9 – Wing discretization for the LL method

The root vortex is dampened by a weighting factor (ω_{FVF}) which considers to what degree the root Γ_{fvf} is suppressed by a wall. For no gap at the root, $\omega_{FVF} = 0$, and if a large gap is present $\omega_{FVF} = 1$. Induced velocity is calculated by:

$$V_{indC} = \frac{-1}{4\pi}\sum_{i=1}^{N}\frac{\Gamma_i - \Gamma_{i-1}}{Z_i - Z_{i-1}} ln(\frac{Z_i - Z_{Cj}}{Z_{i-1} - Z_{cj}}) + \omega_{FVF}\frac{\Gamma_0}{4\pi}\frac{1}{z_0 - Z_{Cj}} + \frac{-\Gamma_N}{4\pi}\frac{1}{Z_N - Z_{Cj}}$$

Vortex strength is calculated from the equation below. 2D section lift coefficients must be known in advance and are a function of effective angle of attack and Re number. Since V_{indC} and Γ_i are coupled, the solution is found iteratively using under relaxation to achieve convergence (Graf, et al., 2014). Once the effective AoA is found, the drag can be calculated from tabulated 2D profile C_D values.

$$\Gamma_i = \frac{1}{2} v_{ind_i}\, c_i\, C_{L_i}(AoA_i - \frac{v_{ind_i}}{AWS_i}, Re_i)$$

This method was implemented in the form of a Python script with user inputs for different wing profiles, plotting options, wind shear assumptions and vortex weighting factors. The Pandas Python module was used as it provided fast and powerful data storage and manipulation tools. Wingsail profile data containing x and z coordinates discretized the wing into 90 panels of approximately 0.26 m in height. The C_L and C_D values from 2D RANS were non-dimensionalised by Re number to account for changes in chord length and AWS along the span.

A function was written to read the 2D RANS values and create a cubic surface of AoA against β via least squares regression. To aid with the surface fitting, coefficients are only plotted up to stall. Beyond stall the code assumes large decreases in C_L and large increases in C_D in the form of an equation. However, such large AoA's are not expected to give optimal profile shapes. The induced wind loop, see Figure 10, uses this surface to find corresponding coefficients for each profile from its effective AoA and β before multiplying this by the local Re number. After induced wind is calculated, the lift and drag contributions of each profile are calculated from their associated coefficients. F_D and F_S are calculated from the boats AWA and integrated along the span. H_M and the height of CoE are subsequently found. Predictions took ~8 seconds on a standard laptop.

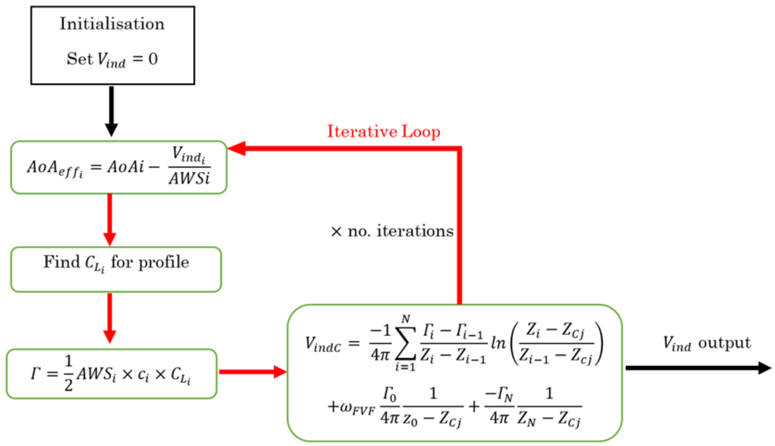

Figure 10 – Iterative loop for calculating induced wind at each profile height

Machine Leaning Surrogate Model

Results from the LL code were used to train a machine learning algorithm producing a surrogate model of the wingsail that could efficiently predict performance using several input variables. Scikit-learn, an open source, widely used machine learning library for Python offered the necessary tools for implementing this. The Kernel Ridge regression (KRR) model was chosen as it provided support for multi-variate regression and had capability for polynomial mapping (Scikit-Learn, n.d.). KRR combines standard ridge regression and the kernel method for pattern analysis. Firstly, the LL data is split into two sets, a training dataset, and a test dataset. This is essential for unbiased evaluation of prediction performance. The training to test split is 3:1, see Figure 11.

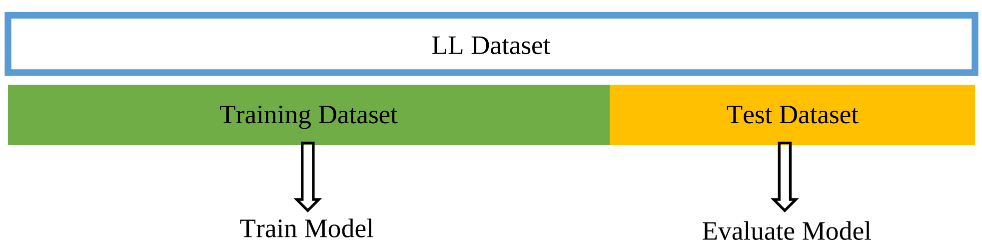

Figure 11 – Training to testing data split

The KRR model learns the relationships between the AoA, camber, twist, F_D, F_S, and H_M for a given TWA and TWS. The accuracy of the model can be evaluated by looking at the coefficient of determination, R^2 value. The maximum value of R^2 is 1, with a higher score resulting in a better fit. The model is compared against the known test data and scores are compared. For an accurate surrogate model, sufficient training data is needed and hence this is where the previous approach of a LL code is useful. Training the model from 3D RANS data would be computationally expensive given the vast number of different wingsail configurations that would need to be evaluated. The best training set size can be determined by looking at the learning curve of the model. A learning curve shows the validation and training score of the model for varying numbers of training samples. It is a useful tool for finding out how much benefit there is from adding more training data and whether the estimator suffers more from a variance error or a bias error (Scikit-Learn, n.d.). Once the model has been trained to sufficient accuracy, predictions of F_D, F_S and H_M can be made from three inputs, see Figure 12. Once trained, typical model predictions took < 0.001 seconds which is over 8000 times faster than the LL code.

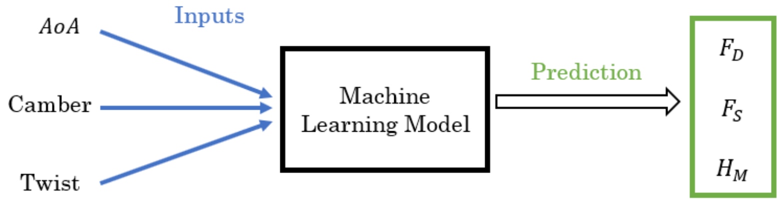

Figure 12 – Model inputs and predicted outputs using KRR model

RESULTS AND DISCUSSION

2D CFD Coefficients

Initially, time averaged RANS simulations were employed to obtain 2D section results. On inspecting the data it was evident that stall was predicted very low at 8° AoA and the residuals showed poor closure of the Navier-Stoke equations. This is partly due to the complex flow that occurs through the slot which influences flow attachment on the trailing flap (Graf, et al., 2014). Therefore, unsteady RANS were chosen to give more accurate results and give better predictions of stall. This meant simulation times were longer, at approximately 16 minutes, but the results could be better trusted. Figure 13 shows C_L and C_D for a range of flap angles and AoAs. β ranges from 0° to 30° and AoA is plotted up to stall. Unsurprisingly as β increases, C_L for a given AoA increases and stall occurred earlier, agreeing with the findings of (Chaill, 1949).

All flap angles show a linear region between -8° and 12° but it's worth noting that for $\beta > 10°$, C_L stays positive even at an AoA of -8° due to the asymmetry of the profile. Stall occurs between 13.5° and 15° after which the simulations have stopped due to poor RANS convergence. In total over 200 2D RANS simulations were conducted equating to approximately 54 CPU hours. There is an expected quadratic increase in drag against increasing AoA between -8° and 13°, after which the drag increases at a rapid rate close to stall. Increasing β results in a larger C_D for the same AoA except for at $\beta = 0°$ which gives larger values of C_D compared to larger flap angles at a negative AoA caused by the symmetry of the profile resulting in the C_D curve being mirrored in the y axis about 0° AoA.

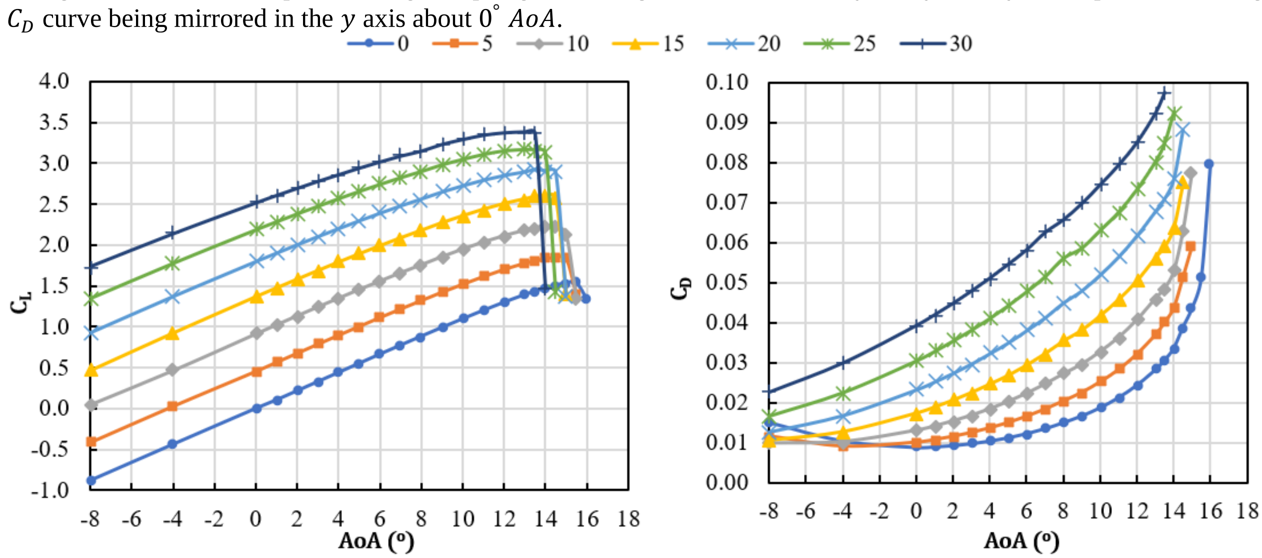

Figure 13 – C_L and C_D against AoA for different β's up to stall

The lift to drag ratio (L/D) for each β is plotted against AoA in Figure 14, and the maximum L/D ratio at each flap angle is overlaid. Knowing the relationship between L/D ratio and β is important in understanding the trade-offs when searching for extra lift. Figure 14 shows that by increasing β, the AoA at which maximum L/D occurs, decreases until a maximum achievable L/D for the section is hit. This occurs at ≈ -5° AoA and $\beta \approx 22.5°$. The change in AoA up the wing caused by wind shear suggests small amounts of wing twist are preferable to maintain optimal section performance. It is worth noting, however, that for finite span lifting surfaces the L/D ratio is likely to be dominated by the induced drag. Therefore, while the 2D L/D ratios are higher than what is expected for 3D, the trends are still likely applicable.

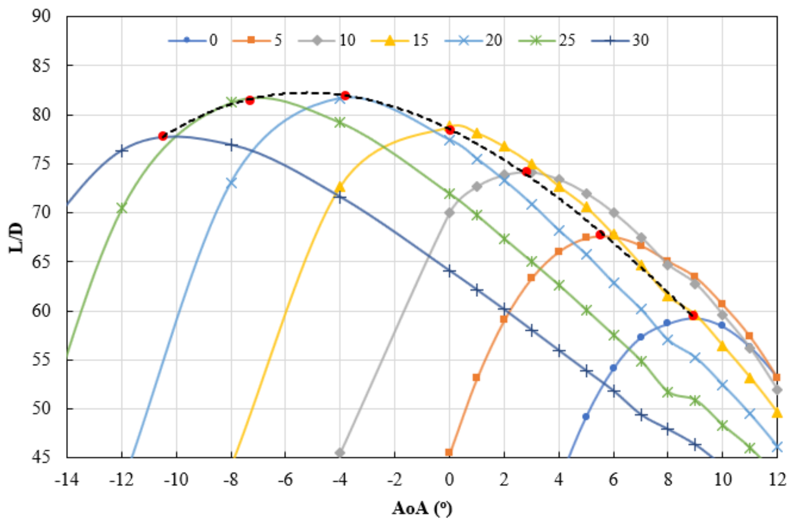

Figure 14 – L/D ratio for different flap angles and AoA.

Velocity contours and streamlines at 10° AoA and varying flap angles are shown in Figure 15 to illustrate the flow around the wing. By increasing β, the velocity on the leeward leading edge of the main element increases and the stagnation point for both elements shifts aft. At smaller flap angles, airflow is restricted through the slot matching the findings in (Grassi, et al., 2013) (Turnock, et al., 2014) (Smith, 1975). At larger flap angles of 20° and 30°, the relative AoA of the flap is 30° and 40°respectivly. At such large AoA, separation would be expected, however, the slot channels flow from the high-pressure side to the low-pressure side as seen by the streamlines, this delays separation on the trailing flap in accordance with the literature. This flow phenomenon allows the large L/D ratios to be achieved.

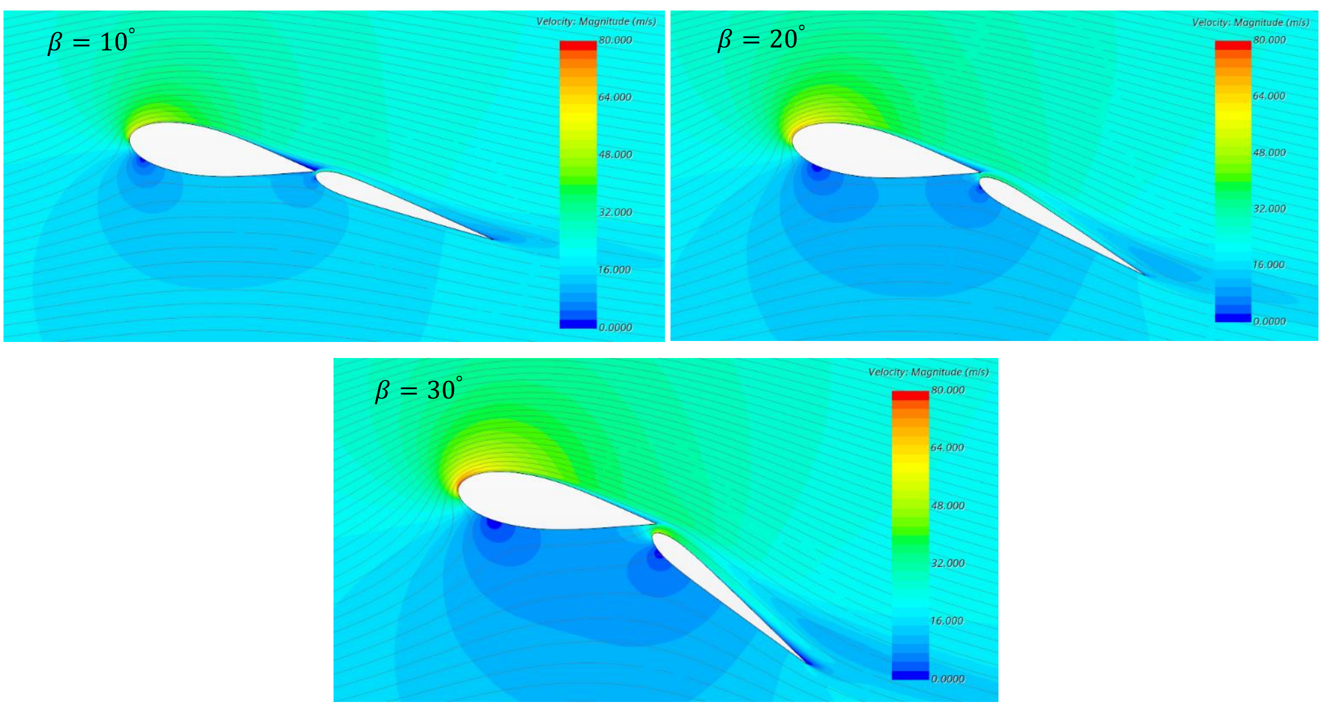

Figure 15 – Velocity plot and streamlines at 10° AoA for $\beta =$ 10°, 20° and 30°

Assuming an AWA of 12° for an upwind case, F_D is plotted against F_S in Figure 16 from -8°AoA up until stall for a range of flap angles to view the relationship. Figure 16 shows that for each β there is a linear relationship between F_D and F_S. Unsurprisingly, as β increases, the forces produced also increase. The gradient of this linear trend is 1.9 meaning that for every increase in F_D, F_S approximately doubles.

Therefore, the limit of H_M is quickly reached and ways of depowering the wing are needed. What is noticeable is that the same values of F_D are possible to achieve with different β operating at different AoAs. For optimal wingsail performance, large driving forces generated by large flap angles are desirable low in the wing whereby the penalty paid in H_M caused by increased side force is reduced due to the smaller lever arm on the yacht.

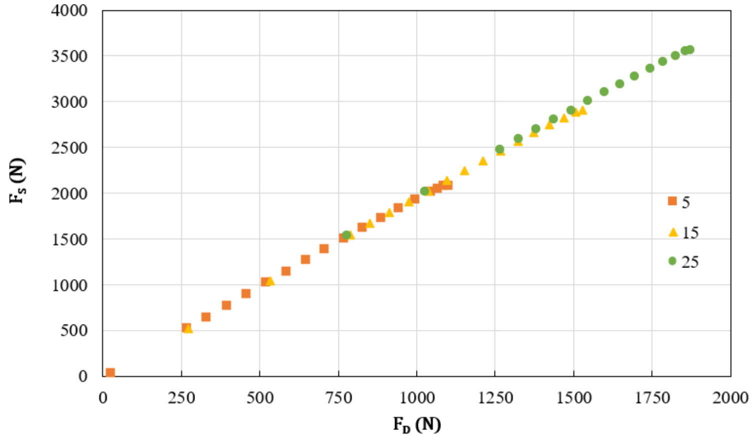

Figure 16 – F_D vs F_S for $\beta = 5^\circ, 15^\circ$ and 25°

Lifting Line Model

Figure 17 shows how varying twist changes F_D, F_S and CoE height. The results presented are for an upwind case in 12 knts TWS at 60° TWA with 31.6 knts of boat speed, as per typical F50 upwind performance. F_D is represented by the lines on the left of the graph and F_S on the right. Increasing the twist reduced the CoE height as expected. As twist is increased, not only is $F_{S\,max}$ reduced, but this maximum occurs at a lower location. This confirms that twist is a powerful tool for reducing H_M in accordance with (Collie, et al., 2015) (Whidden & Levitt, 2016) (Graf, et al., 2014). Furthermore, the increase in twist, reduces the maximum value of F_D and shifts the distribution to lower down the wing subsequently reducing the pitching moment and improving the boats longitudinal stability. With 35º of twist, F_S changes sign at 87% span indicating that the top 13% of the wing is producing positive righting moment.

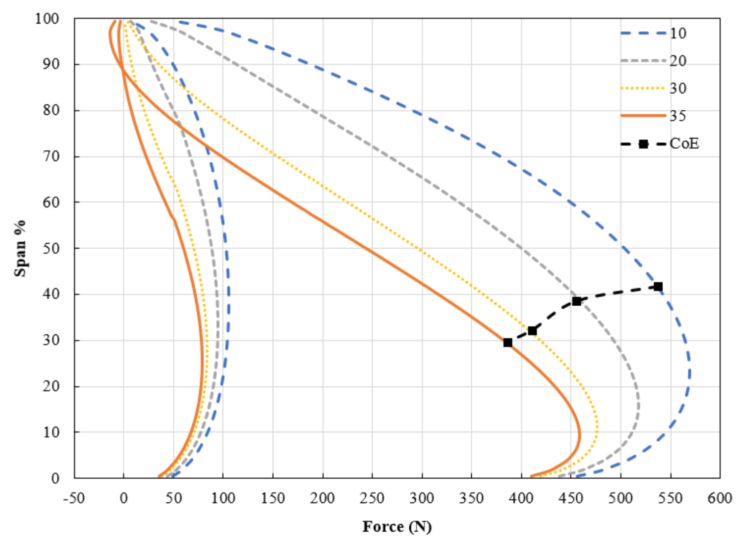

Figure 17 – F_D (left) and F_S (right) distribution for wing at 4° AoA, 20° camber and varying twists

Figure 18 shows the relationship between F_D and H_M in 12 knts TWS at 60° TWA for different camber configurations. The twist is kept constant at 20° and each point represents an AoA which ranges from -1 to 3°. The relationship between F_D and H_M is approximately linear for each camber configuration. As camber increases, the values of F_D and H_M increase and follow the trend from the previous configuration. There are points where different cambers will give similar values of F_D and H_M just at different AoAs. An example of this is at -1° AoA for 15° camber and, -3° AoA for 10° camber. The same relationship was also shown above for F_D and F_S in Figure 16.

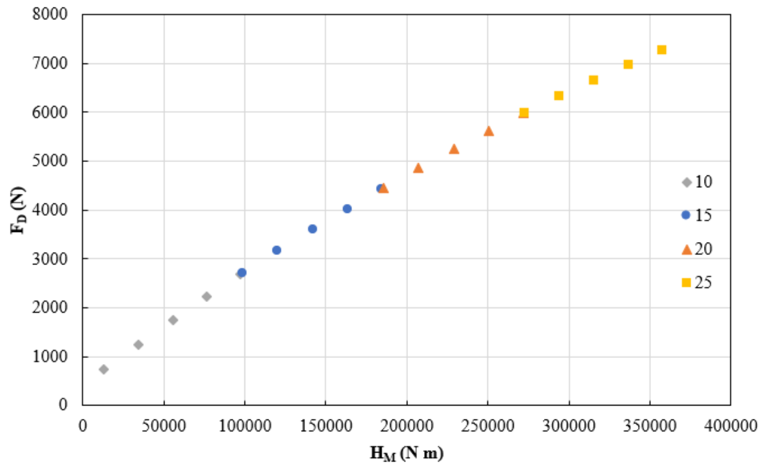

Figure 18 – F_D vs H_M for different AoA's and camber configurations

Interestingly, at higher camber configurations, the range of F_D decreases for the same range of AoAs, see Table 6. This suggests that at smaller cambers, the change in F_D is more sensitive to changes in wing AoA. Therefore, lower camber configurations are less forgiving to changes in AoA caused by wing sheet movement. However, this is only considering the case where twist is kept constant for all cambers.

Table 6 – Change in F_D for different cambers between -1° ≤ AoA ≤ 3°

Camber Setting (°)	10	15	20	25
ΔF_D (N)	1935	1730	1521	1282

3D CFD Comparisons

For initial comparisons wind shear was excluded from the CFD results to simplify the model setup. An assumption of the root being end plated to the deck has been made, allowing little to no pressure loss from the leeward to windward side. Increasing ω_{FVF} results in larger losses of lift at the root and increases induced drag. Initial comparisons for a wing with 0° camber and 0° twist showed that a $\omega_{FVF} = 0.1$ gave the closest trends against C_L, C_D, CoE, and moment coefficient (C_M) when compared to other ω_{FVF} factors, see Figure 19. Higher ω_{FVF}'s gave better predictions of C_D but compromised C_L, C_M and CoE predictions.

On average the LL gave a difference of -5% C_L and -20% C_D from 2° ≤ AoA ≤ 14° demonstrating how powerful the LL is when computational speed is a priority, see Figure 19. A single LL prediction took ≤8 seconds on a laptop, compared to a 3D simulation that took ~6 hours. At $AoA's \geq 15°$ the LL began to deviate from the CFD results by overestimating lift and underestimating drag. This is likely due to flow separation that occurs close to stall being poorly captured by the LL, agreeing with the findings of (Graf, et al., 2014).

Comparisons with C_M show an average difference of -10%. With increasing AoA the difference becomes larger with the reasons stemming from the smaller lift and drag predictions above. Figure 19 shows CoE height is a more sensitive result than C_M because it is affected by the shape of the lift distribution. As AoA increases, CoE is expected to rise and this can be seen in the CFD. Strangely this does not occur with the LL, whereby the CoE reduces in height. On average the difference in predicted CoE is -8% and indicates a difference in lift distribution.

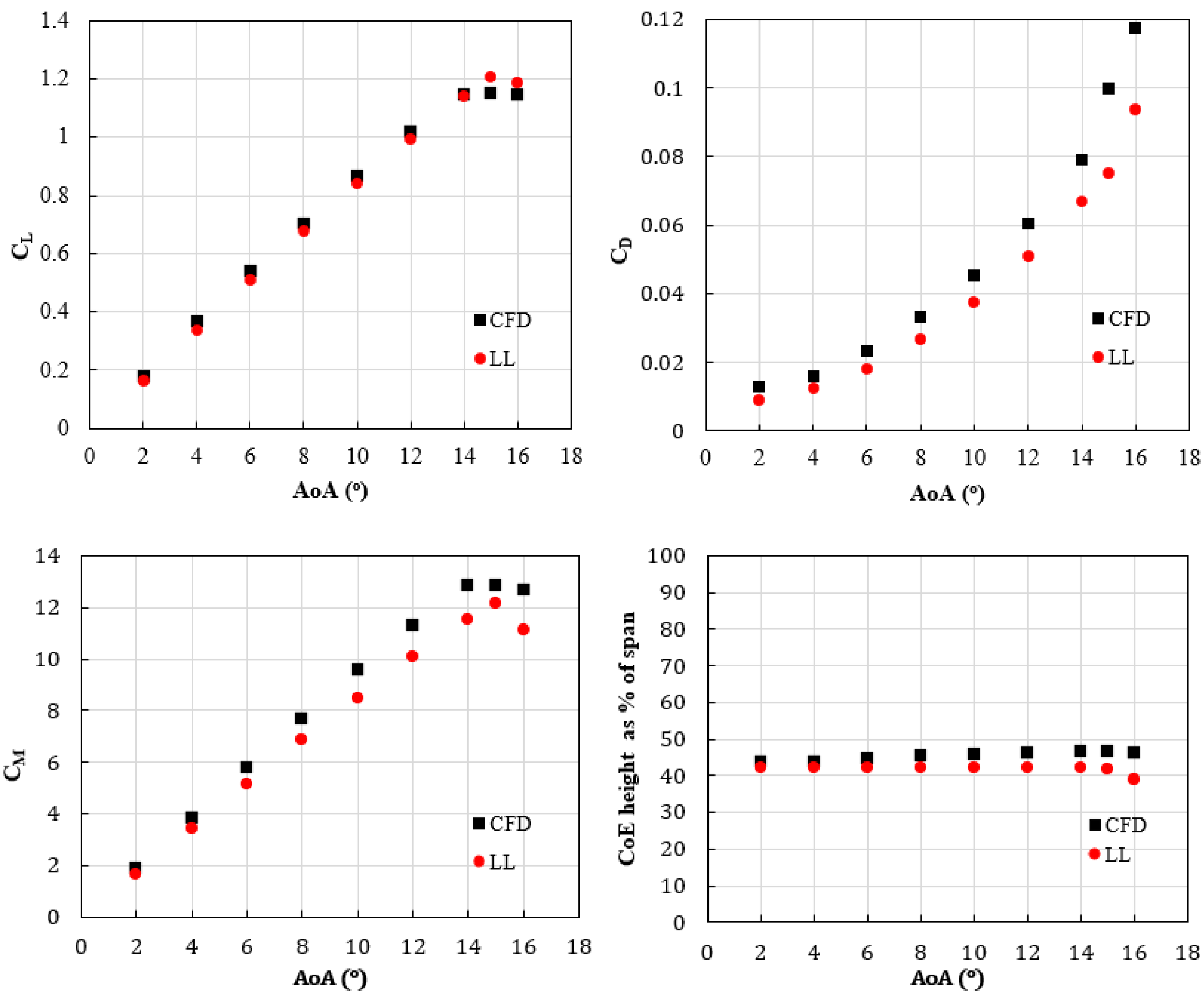

Figure 19 – C_L, C_D, C_M and CoE against AoA for both LL and CFD (0° camber, 0° twist)

The LL is overestimating the tip washout causing a lower percentage of lift predicted at the wing tip, causing the CoE to be lower, see Figure 20. The LL predicts higher lift than the CFD up to 60% span. Beyond 60% span, the LL shows a rapid decrease in spanwise load towards the tip caused by the underprediction of downwash. Empirical corrections by (Molland & Turnock, 2021), and increases in ω_{FVF} gave improved spanwise loading but did not translate into better overall prediction of C_L and C_D. The presence of tip and root vortices is shown in Figure 21.

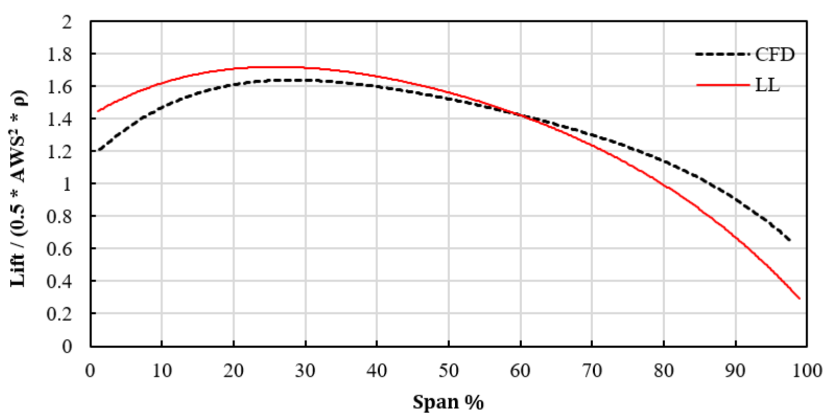

Figure 20 – Spanwise C_L distribution for both CFD and LL

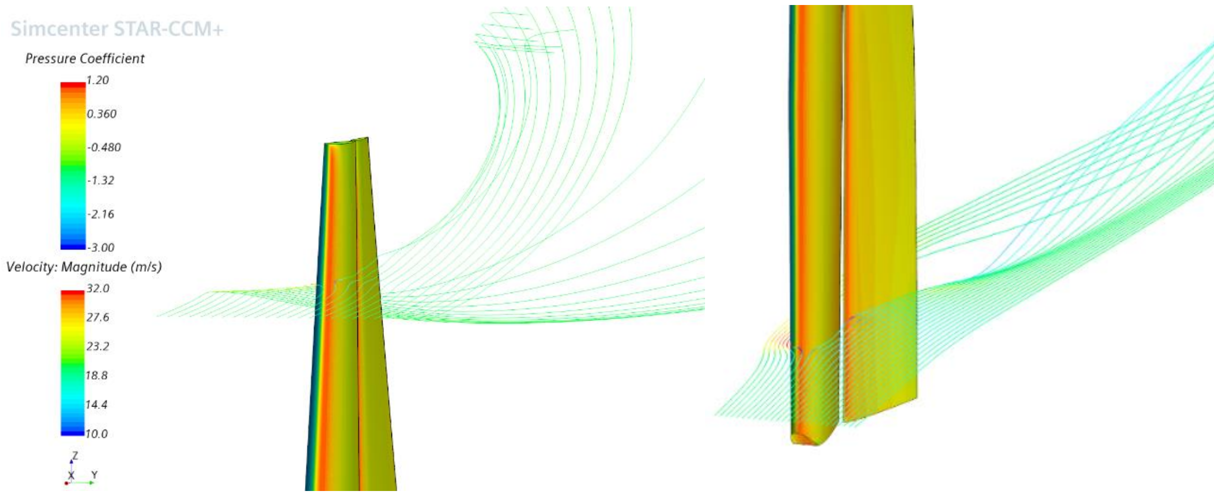

Figure 21 – Pressure coefficient and streamline plot showing the tip and root vortex

The driving force and heeling moment are plotted for $2^{\circ} \leq AoA \leq 15^{\circ}$ in Figure 22. Up to 14° AoA, the LL underpredicts H_M on average by 5% and overpredicts F_D by 1% showing impressive accuracy. Past 14° the wing starts to stall and so there is a drop in F_D meaning that sheeting the wing in further is counterproductive as H_M remains high. This is not predicted by the LL and once again shows it's limitations at high AoA's. Overall the trends of C_L, C_D and C_M match up for both CFD and LL predictions, therefore there can be confidence in the LL code allowing wingsail optimisations to be carried out. With more investigation the accuracy can be improved by factoring in additional corrections to the LL model.

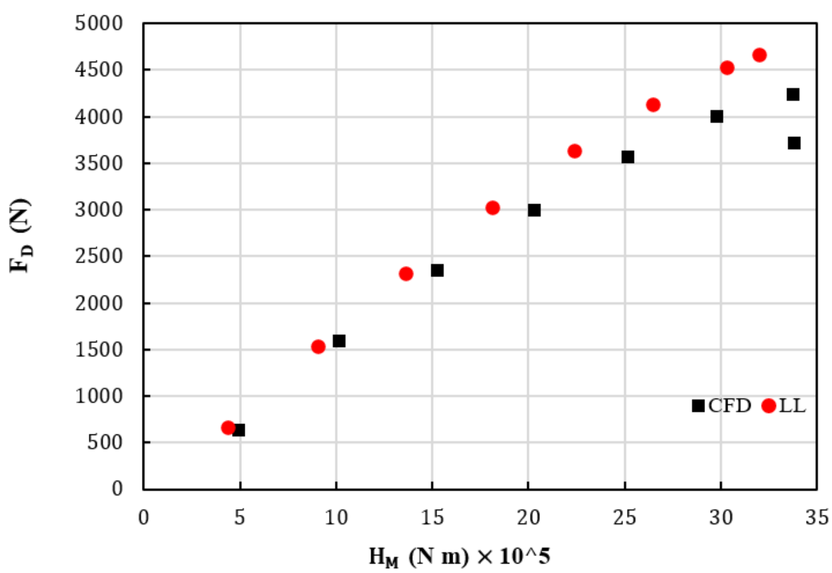

Figure 22 – F_D against H_M for both LL and CFD at $2^{\circ} \leq AoA \leq 15^{\circ}$

Surrogate Model

Using the LL model, a sweep of AoA, camber and twist configurations were conducted to produce a dataset of results. The size of this dataset was varied to investigate the influence of training set size on performance for different order KRR models. The learning curves for each order model are seen below in Figure 23. Both the mean and standard deviation of scores are shown. Different training set sizes ranging from 100 to 1000 were tested. The LL allows such large data sets to be created for a relatively cheap computational cost. 1000 LL evaluations took approximately 2.2hrs which is vastly quicker than if the data were to come from 3D RANS simulations.

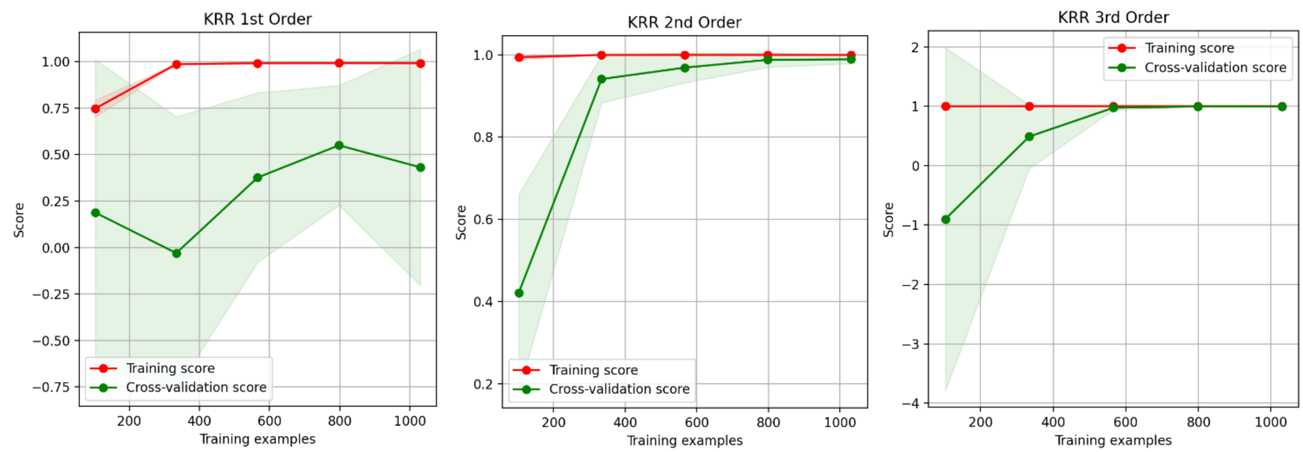

Figure 23 – Learning curves for 1st, 2nd and 3rd order KRR models

For the first order model, cross validation scores are low with a high variance for a range of training sizes showing that the first order approximation is not a good choice. For small numbers of training data, the 2nd order model scores much higher and has a smaller standard deviation suggesting it is a much better fit than the 1st order model. Adding more training samples will most likely increase generalisation whereby the score converges just below 1 with a sample size of 1000. The 3rd order model shows the worst performance with small training sizes but quickly converges to a score of 1 with just 566 training points, after which the model does not benefit from more training data. The 3rd order model has the longest fit times of ~0.05s when compared to the 1st and 2nd order models, but this time is negligible when compared to LL evaluations. Once built, predictions from the model take even less time at ~0.001s showcasing its attractiveness for implementation into VPPs. Other regression models were not investigated due to time limitations, but full comparisons of other techniques would be interesting to investigate, especially when using data with non-linear wing twist profiles whereby the relationships between input and output might not be so straightforward. In this study the 3rd order model was chosen with 900 data points for training giving an R^2 value of 0.999.

OPTIMISATION

Compute Resource

Table 7 shows the computational resource and time taken for each method discussed. The 3D CFD takes the most time at ~6 hours per simulation and requires the most compute resource by a large margin using the University of Southampton's HPC cluster. 2D CFD took slightly less time at ~ 16 minutes per simulation but can be run at much higher fidelity. Ultimately the 2D simulations are necessary as the LL code is dependent on them, however, once the sectional information is obtained the number of different wing configurations that can be predicted is endless. Arguably the CFD runs can be run in parallel which would shorten the time taken for multiple evaluations, but the computational resource needed remains comparable.

Table 7 – Computational cost for each method

Method	Machine	Available Resource	CPU Time (1 sim)	CPU Time (500 sims)
2D CFD	HPC	× 3 2.0 GH_z Intel Xeon 120 cores, 486 GB Ram	~16 mins	~5.6 days
3D CFD	HPC	× 3 2.0 GH_z Intel Xeon 120 cores, 486 GB Ram	~360 mins	~125 days
LL code	Laptop	2.2 GH_z Quad-core Intel i7 16 GB Ram	~8 s	~1 hr
Machine Learning Surrogate Model	Laptop	2.2 GH_z Quad-core Intel i7 16 GB Ram	~0.001 s	~0.5 s

A single simulation using the LL code took ~8s which is over 2700 times faster than a 3D CFD simulation. This time saving is impressive and when scaled up to 500 simulations, the saving speaks for itself. The physical cost of such computation, which can be broken down into the cost of components, operation/maintenance, and price of electricity, would be substantially higher than that of a desktop PC. Once the LL model has been leveraged to produce a large sparse data set of wingsail profiles, the machine learning algorithm can be trained producing a surrogate model of the wing. An exhaustive search in a fraction of the time is now possible and implementation of this model into a VPP would be the next logical step.

Upwind Profile Optimisation

The LL code is set to produce a sparse set of data points of different wingsail profiles. The goal is to have enough data points so that the machine learning algorithm can accurately interpolate the data. Using the surrogate model, an exhaustive sweep is possible due to its computational speed. Results that exceed H_M constraints are filtered out and then profiles giving the largest drive force are presented. An optimum wing shape is to be found for an upwind case at 60° TWA in 12 and 16 knts TWS. Wind shear is considered, and a linear twist profile is assumed for the optimisation. The data input to the LL code is shown in Table 8. After speaking with designers from SailGP, a H_M limit of 18 $T\ m$ has been set.

Table 8 – Data input to LL model

Input	Case 1	Case 2
TWS	12 $knts$	16 $knts$
TWA	60°	60°
V_s	31.6 $knts$	39.6 $knts$
Leeway	3.15°	3.26°
H_M limit	18 $T\ m$	18 $T\ m$

Results

The LL produced 1200 data points for each case taking a time of ~2 hours. The machine learning algorithm then interpolated the data with an R^2 value of 0.999, showing an extremely accurate model fit. The algorithm performed an exhaustive sweep with $0^{\circ} \leq$ camber $\leq 30^{\circ}$, $0^{\circ} \leq$ twist $\leq 50^{\circ}$, and $-5^{\circ} \leq AoA \leq 7^{\circ}$. 14500 different wing profiles were evaluated in an impressive 2.85 seconds. A polar plot of the maximum F_D for the given H_M constraint is plotted from 40° to 90° TWA for both wind speeds in Figure 24.

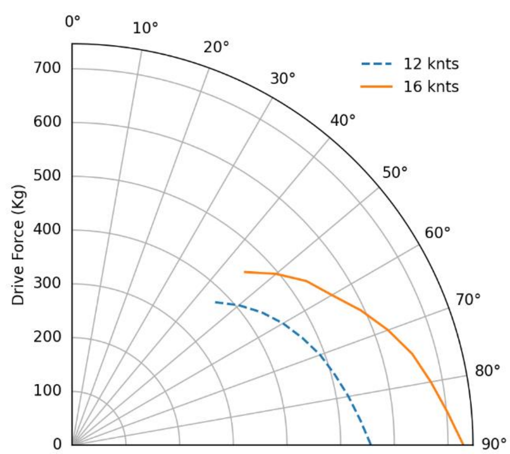

Figure 24 – Polar plot of maximum F_D against TWA for 12 and 16 knts TWS

Table 9 shows results of the optimum profiles found. The profiles were entered into the LL to check interpolation accuracy of the algorithm. The algorithms output was within 0.5% of the LL predictions proving accurate interpolation had been achieved. For Case 2, the profile found had less camber and more twist compared with Case 1. This is expected as the AWS is higher in Case 2 and hence the wing needs depowering more to not exceed the H_M constraint. The increased twist reduced the CoE by 1.86 m and meant the top 20% of the wing was providing positive R_M. This allowed for a higher overall drive force to be achieved, see Figure 25.

Table 9 – Optimum profiles found via the surrogate model

	Case 1	Case 2
AoA	2°	2°
$Camber$	20°	18°
$Twist$	28°	34°
F_D	$446\ kg$	$552\ kg$
F_S	$2263\ kg$	$2932\ kg$
H_M	$17.9\ T\ m$	$17.8\ T\ m$
CoE	$7.91\ m$	$6.05\ m$

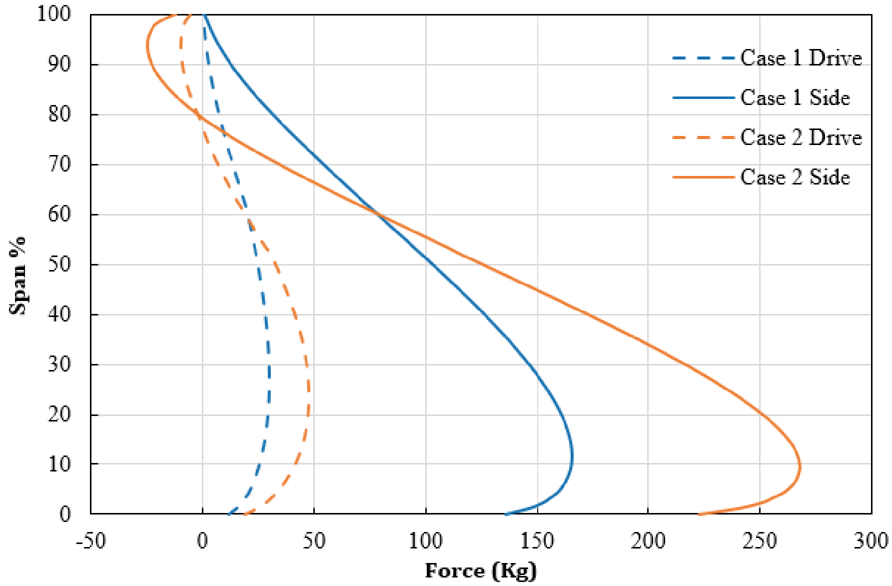

Figure 25 – Distribution of F_D (dashed) and F_S (solid) against % span

Final CFD Comparison

A final 3D simulation implementing a twisted inflow velocity was conducted to compare results for Case 1. Table 10 shows the output from the CFD along with the LL model prediction.

Table 10 – CFD and LL comparison of optimised profile at 60° TWA in 12 knts TWS

	CFD	LL Model	% Difference
F_D	$486\ kg$	$446\ kg$	-8.2
F_S	$2272\ kg$	$2263\ kg$	-0.4
H	$17.7\ T\ m^{-1}$	$17.9\ T\ m^{-1}$	1.1
CoE	$7.82\ m$	$7.91\ m$	1.2

The prediction of H_M and CoE height was close with the LL model overpredicting by 1%. The F_S prediction was even closer at -0.4%. There was a larger difference in F_D with the model underpredicting by 8%. Figure 26 show the pressure coefficient on the surface of the wingsail along with streamlines depicting the flow at the root and tip. There is a large negative pressure coefficient close to the leading-edge showing an increase in air speed over the leeward side. The pressure coefficient decreases along the span also indicating that less lift is being produced near the tip, because of the wing twist.

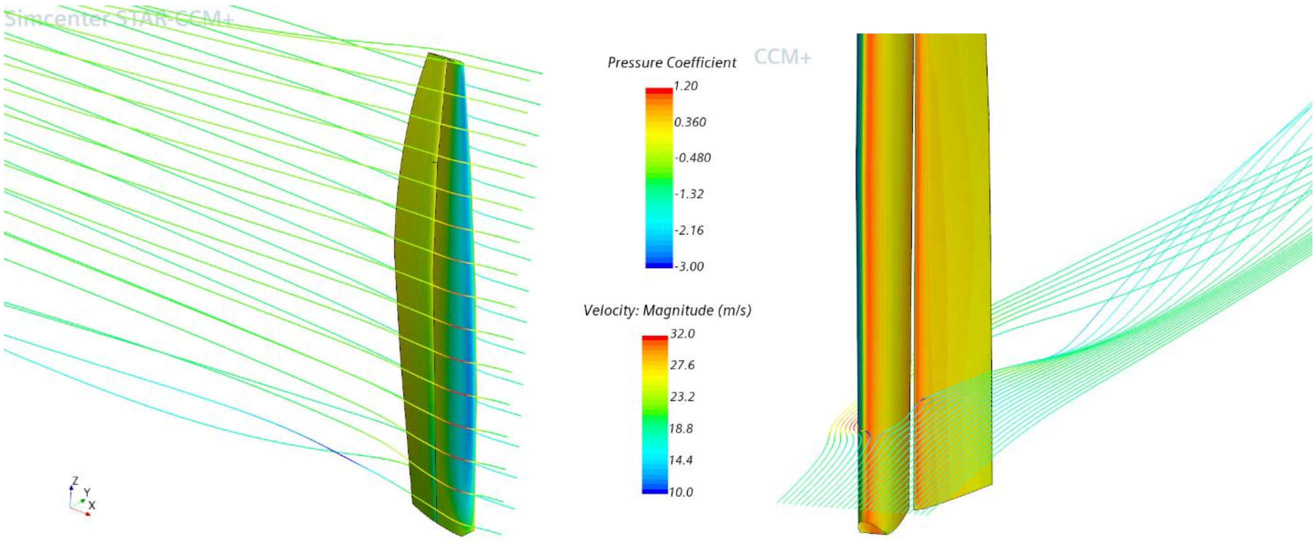

Figure 26 – Pressure coefficient and streamline plot of the wing for Case 1 showing large negative pressure coefficients on leading edge and influence of root vortex

CONCLUSION

In summary, a computationally efficient approach for finding optimum wingsail profiles has been developed. A range of different methods have been used to show that computationally fast code run on a laptop can adequately predict wingsail performance when compared to expensive 3D CFD executed on a HPC cluster. This method isn't a substitute for existing approaches but offers a solution to select design areas that could then be investigated more thoroughly with 3D RANS or similar. The speed of this method would also allow this to be integrated within a VPP where full yacht optimisation could be carried out. The project has shown that:

i.) Unsteady RANS simulations give improved flow predictions when finding 2D section data of wingsails. Steady RANS simulations give poor CFD residuals convergence, predict stall earlier, and give lower values of $C_{L\,max}$.
ii.) Resolving lift and drag forces into F_D and F_S show a linear relationship between the two up to stall.
iii.) Using 2D profile data of the wingsail, a LL model taking ~8 seconds per simulation on a laptop, can predict F_D and H_M within 1% and 5% respectively when compared to 3D RANS simulations taking 6 hours on a HPC cluster. This gives confidence in using the model for wingsail optimisation.
iv.) For fixed wing profiles, increasing the AoA results in a linear increase in F_D and H_M up to stall. For a fixed value of twist, lower camber configurations result in F_D being more sensitive to changes in AoA caused by wing sheet movement.
v.) A simple machine learning algorithm can produce an accurate surrogate model using LL data, giving predictions within 0.5%. This accuracy allows exhaustive wingsail profile sweeps 8000 times faster than the LL code demonstrating the power of leveraged surrogate models.
vi.) The combined LL and machine learning algorithm approach provides an efficient and powerful tool for evaluating a large number of different wingsail configurations with acceptable levels of accuracy.
vii.) Using the approach, optimum wingsail profiles polars can be found for a range of TWA and TWS, accelerating the learning of new teams, designers and sailors ultimately improving yacht performance.

ACKNOWLEDGMENTS

Firstly, I would like to thank my supervisors Prof Stephen Turnock and Dr Martyn Prince for their continued support and guidance throughout the project. They have given me a wealth of knowledge and directed me towards best practices that have helped structure this paper.

Secondly, I would also like to thank Raphael Censier, Tom Herbert-Evans, David Hazzard and Mike Drummond from SailGP who have provided me with the necessary wingsail and VPP data. Their willingness to help has been invaluable.

In addition, I would like to thank Prof Kai Graf from the Kiel Yacht Research Unit for his insight and help on the lifting line theory.

Finally, I want to thank Dr Elena Vataga from the High-Performance Computing team at Southampton University who has been incredibly helpful in answering questions and giving advice when using the Iridis 5 computing cluster.

REFERENCES

Chaill, J. F., 1949. *Summary of Section Data on Trailing Edge High Lift Devices,* s.l.: US Gov.

Claughton, A., 1998. *Sailing Yacht Design.* s.l.:Addison Wesley Longman Limited.

Collie, S., Fallow, B., Hutchins, N. & Youngren, H., 2015. Aerodynamic Design and Development of AC72 Wings. *5th High Performance Yacht Design Conference 2015,* pp. 15-24.

Graf, K., Hoeve, A. & Watin, S., 2014. Comparison of full 3D-RANS simulation with 2D-RANS/lifting line method calculations for the flow analysis or rigid wings for high performance multihuls. *Ocean Engineering,* Issue 90, pp. 49-61.

Grassi, C., Foresta, M., Lombardi, G. & Katz, J., 2013. Study of Rigid Sail Aerodynamics. *International Journal of Small Craft Technology,* Volume 155.

Houghton, E., 2013. *Aerodynamics for Engineering Students.* s.l.:Elsevier.

Menter, F. R., 1994. Two-equation eddy viscosity turbulence models for engineering applications. *AIAA Journal,* 32(8).

Molland, A. & Turnock, S., 2021. *Marine Rudders, Hydrofoils and Control Surfaces: Principles, Data, Design and Application.* s.l.:Butterworth-Heinemann.

Peart, T., Aubin, N., Nava, S. & Norris, S., 2021. Multi-Fidelity Surrogate Models for VPP Aerodynamic Input Data. *Journal of Sailing Technology,* 6(1), pp. 21-43.

Scikit-Learn, n.d. *Kernel Ridge.* [Online]
Available at: https://scikit-learn.org/stable/modules/kernel_ridge.html
[Accessed 21 April 2021].

Sheldehl, R. & Klimas, P., 1981. *NACA-0012 Airfoil Section Data from: Aerodynamic Characteristics of Seven Airfoil Sections through 180-Degree Angle of Attack,* s.l.: Sandia National Laboratories Energy Report.

Siemens Digital Industries Software, 2020. *Star-CCM+ User Guide 15.06.007-R8,* s.l.: s.n.

Smith, A. M., 1975. High Lift Aerodynamics. *Journal of Aircraft,* 12(6).

Turnock, S., Campbell, I. & Magherini, M., 2014. Parameters Affecting the Performance of the C-Class Wingsail. *Transactions of the Royal Institution of Naval Archtects Part B: International Journal of Small Craft Technology,* Volume 156, pp. 21-34.

Whidden, T. & Levitt, M., 2016. *The Art and Science of Sails.* Maine: Seapoint Books and Media.
Wood, C. & Tan, S., 1978. Towards an optimum yacht sail. *Journal of Fluid Mechanics,* 85(3), pp. 459-477.